Cross Shock Electrostatic Potentials at Mars Inferred From MAVEN Measurements

Shaosui Xu, Steven J. Schwartz, David L. Mitchell, Konstantinos Horaites,
Laila Andersson, Jasper Halekas, Christian Mazelle, Jacob R. Gruesbeck

HAL Id: insu-03672448
https://insu.hal.science/insu-03672448

Submitted on 9 Dec 2022

JGR Space Physics

Key Points:
- Electrostatic cross-shock potential at Mars varies systematically with solar zenith angle and magnetic latitude
- Shock potential scales with incident ram ion energy and is affected by magnetosonic Mach number
- We find that the cross-shock potential depends little on several other plasma parameters

Supporting Information:
- Supporting Information S1

Correspondence to:

S. Xu,
shaosui.xu@ssl.berkeley.edu

Cross-Shock Electrostatic Potentials at Mars Inferred From MAVEN Measurements

Shaosui Xu[1] , Steven J. Schwartz[2] , David L. Mitchell[1] , Konstantinos Horaites[2] , Laila Andersson[2] , Jasper Halekas[3] , Christian Mazelle[4] , and Jacob R. Gruesbeck[5]

[1]Space Sciences Laboratory, University of California, Berkeley, Berkeley, CA, USA, [2]Laboratory for Atmospheric and Space Physics, University of Colorado, Boulder, Boulder, CO, USA, [3]Department of Physics and Astronomy, University of Iowa, Iowa City, IA, USA, [4]IRAP, CNRS, University of Toulouse, UPS, CNES, Toulouse, France, [5]Goddard Space Flight Center, Greenbelt, MD, USA

Abstract A bow shock is generated by the interaction of the solar wind with the planetary global dipole field (e.g., Earth), or with (mainly) the planetary ionosphere (e.g., Mars). The cross-shock potential has been well studied at Earth but not yet for Mars. We infer and approximate the peak in the frame invariant de Hoffmann-Teller shock potential profile at Mars (ϕ) with data from the Mars Atmospheric and Volatile EvolutioN (MAVEN) mission. We find that ϕ and its ratio to the solar wind ram ion energy ($E_{\rm ram}$) vary similarly against solar zenith angle (SZA, a proxy for the angle between the solar wind flow and the shock normal) and magnetic latitudes. Our results also reveal no significant dependence of the shock potential on parameters such as the angle between the upstream interplanetary magnetic field (IMF) and the shock normal and plasma beta of upstream solar wind. There is a somewhat positive correlation with the magnetosonic Mach number and the magnetic amplification ratio across the shock. We also find a solar cycle effect on the shock location, closer to the planet near the solar minimum, as expected. Lastly, similarities and differences of cross-shock potentials at Mars and Earth are discussed. Characterizing electron energization and high-altitude ion loss at Mars is influenced by the bow shock and thereby the work here.

1. Introduction

The interaction between the supersonic solar wind flow and planetary intrinsic dipole fields (e.g., Earth, Jupiter, and Saturn) or ionospheres (e.g., Venus, Mars, and comets) results in the formation of a shock wave, or termed as the bow shock. Planets with a strong intrinsic dipole field, thus a strong magnetic pressure, have large stand-off distances at the nose that depend on the strength of the dipole. In contrast, at planetary objects without a global intrinsic field but a significant ionosphere, ion pickup becomes important for this interaction and the standing-off distance for this type of bow shock is much closer to the planet, within two planetary radii for Mars (e.g., Gruesbeck et al., 2018; Trotignon et al., 2006; Vignes et al., 2000) and Venus (e.g., Luhmann, 1986). Many shock properties have been well investigated at Earth (e.g., Formisano, 1974; Wilkinson, 2003) and Mars (e.g., Burne et al., 2020; Gruesbeck et al., 2018; Halekas et al., 2017; Hall et al., 2019; Mazelle et al., 2004; Nagy et al., 2004).

One aspect of the shock properties is the electrostatic field within the shock layer, acting to maintain charge neutrality while initiating processes to slow down the upstream solar wind bulk flow, transforming from a dynamic pressure dominated plasma flow in the upstream to a hot plasma dominated by thermal pressure in the downstream magnetosheath. This electrostatic field, consequently an electrostatic potential crossing the shock, is relatively well studied at Earth (e.g., Dimmock et al., 2012; Feldman et al., 1983; Goodrich & Scudder, 1984; Schwartz et al., 1988; Scudder et al., 1986) but not yet for Mars.

As pointed out by Goodrich and Scudder (1984), the potential change across the shock, that is, the cross-shock potential, is frame dependence due to the Lorentz transformation of the electric field between different reference frames. The two most commonly used frames are the normal incident frame (NIF) and the de Hoffmann-Teller frame (HTF; De Hoffmann & Teller, 1950) , the associated electric fields (along the shock normal, $\hat{\mathbf{n}}$) and potential jumps denoted as $\mathbf{E}_{\mathbf{n}}^{N}$ & ϕ^{N} and $\mathbf{E}_{\mathbf{n}}^{HT}$ & $\phi^{\rm HT}$, respectively. In the NIF, the plasma velocity is collinear with the shock normal upstream of the shock while in
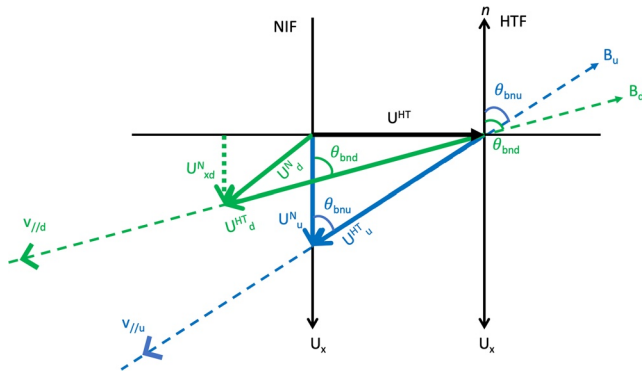
Figure 1. Schematic of transformation between the NIF and the HTF for a planar shock. **U** is the bulk flow velocity, with subscripts "u" and "d" denoting upstream and downstream, and superscripts "N" and "HT" denoting NIF and HTF, respectively. $\hat{x}$ is opposite to the shock normal, that is, $\hat{x} = -\hat{\mathbf{n}}$. θ_{Bn} is the angle between the shock normal and the (upstream or downstream) magnetic field vector. $\mathbf{U}^{HT}$ is the frame transformation velocity. $v_{//}$ is the electron peculiar velocity along the field line in the plasma rest frame.

the HTF, it is transformed such that the flow and the magnetic field are collinear on both sides of the shock. ϕ^{N} and ϕ^{HT} are integrals of $\mathbf{E}_{\mathbf{n}}^{N}$ and $\mathbf{E}_{\mathbf{n}}^{HT}$ along the shock normal direction, respectively. These two potentials differ because in transforming from one frame to another there is a contribution from $\mathbf{U}^{HT} \times \mathbf{B}$, where $\mathbf{U}^{HT}$ is the frame transformation velocity, which lies along the shock front and in the plane containing the upstream **B** and the shock normal. The transformation from the NIF to the HTF is illustrated in Figure 1 or see Figure 1 of Schwartz et al. (2019).

From the electron perspective, in the NIF, they experience the full ϕ^{N} but also drift tangential to the shock surface along the direction of the motional electric field ($-\mathbf{U} \times \mathbf{B}$), losing some of the gained energy. In contrast, in the HTF, the motional electric field vanishes as $\mathbf{U} // \mathbf{B}$ such that electrons only experience ϕ^{HT}. In other words, $\phi^{HT} < \phi^{N}$ and electrons' net energy gain is ϕ^{HT}, which is the main focus of this study. Also, note that because no motional electric field is involved, ϕ^{HT}, as a purely electrostatic potential, is frame invariant and independent of paths of integration but determined by the potential difference between the start and end point. Thus, although $\mathbf{E}^{HT}$ is strictly along the shock normal in steady state, it is common to re-cast ϕ^{HT} by integrating along the magnetic field, exploiting the frame invariance of electric and magnetic fields (Scudder et al., 1986). This also corresponds to the path followed by a magnetized electron through the shock layer in the HTF (assuming a planar shock and thus no curvature drift).

In the HTF, ϕ^{HT} can be directly related to the electron pressure gradient term (∇p_e) via either the generalized Ohm's law or equivalently the electron momentum equation. In the momentum equation, the inertial terms are small due to electrons' small mass and electron bulk velocity being parallel to the magnetic field in the HTF. Neglecting frictions, we thus obtain $\mathbf{E}_{\mathbf{n}}^{HT} = -\nabla p_e / en$, where n is the plasma density and e the elementary charge. As $\mathbf{E}_{\mathbf{n}}^{HT}$ is purely electrostatic, the cross-shock potential ϕ^{HT} can be traced/inferred from the energy gain for electrons in the field-aligned direction. Provided the shock thickness is beyond an electron gyroradius, magnetic moment conservation ensures that there is no redistribution of energy from these perfectly field-aligned electrons into perpendicular velocity components. Our theoretical concepts and analysis are based on steady state shock profiles for which the length scales are large enough that electrons remain magnetized as they traverse the shock (e.g., Savoini et al., 2005; Schwartz et al., 2011). This is typically, though not always the case, at planetary bow shocks. We employ some averaging and selection procedures to minimize the influence of variability in the shock both in terms of the electron response and location. In this study, we approximate the cross-shock potential in de Hoffmann-Teller frame ϕ^{HT} to be equivalent of the electron energization along the magnetic field line (ϕ) measured in the spacecraft frame for simplicity, and will discuss the caveats of such an approach later.

While Meziane et al. (2019) found shock potentials to be close to zero from the energy dependent loss cones of electrons back-streaming from the shock in the upstream, the authors deemed that these electrons were magnetically reflected first before they experience the full shock potential. This study, however, explores the full cross-shock potential at Mars for the first time (to our knowledge) from electrons traversing the shock. The shock potential is inferred from the energy change in electrons crossing the shock, which is a classical way to obtain electrostatic potentials (e.g., Xu et al., 2019, 2020). More specifically, we compare the phase space density of electrons upstream in the solar wind to the distributions throughout the shock layer into the downstream, obtaining the energy gain, or energization, from cross-shock potentials. Electron measurements are provided by the Solar Wind Electron Analyzer (SWEA) instrument (Mitchell et al., 2016) and magnetic field vector measurements by the Magnetometer (MAG) instrument (Connerney et al., 2015), both onboard MAVEN. The characterization of the shock potential at Mars and how it compares with Earth can better our understanding of bow shocks at different planetary objects. It is also important for understanding electron energization at Mars, which is an energy source to the Mars upper atmosphere, and also an important source for high-altitude pick-up ions, partly

produced by electron impact ionization of Mars' hydrogen and oxygen coronae (e.g., Curry et al., 2013; Mazelle et al., 2018).

2. Case Studies

2.1. Case Study: Methodology

To illustrate how we obtain cross-shock potentials from MAVEN data, we take an orbit on April 2, 2018 as an example, as shown in Figure 2. Magnetic fields are shown in the Mars-centered Solar Orbit (MSO) coordinate system, where X points from the center of Mars to the Sun, Z points to the north pole of Mars' elliptical orbit plane, and Y completes the right-handed system. MAVEN was in the upstream solar wind from 20:30 UT (universal time) and encountered the bow shock at ~21:09 UT near the subsolar point (solar zenith angle ~10°), where we see a significant enhancement in the magnetic field amplitude in panel (a) and much hotter electrons in panel (c). We mark the approximate location of the bow shock with the vertical green dashed line but note that the bow shock is a boundary with a thickness (on the order of a few hundred kilometers and preceded by a shock foot formed by a population of reflected solar wind ions, complicated further at Mars by the presence of pick-up ions). The second ramp-up of magnetic strength from 21:13 UT is where MAVEN entered the magnetic pileup region (MPR) and reached the main ionosphere after crossing the photoelectron boundary (PEB; e.g., Garnier et al., 2017; Mitchell et al., 2001) at 21:16:30 UT. We note here the rapid traversal through the non-uniform Martian magnetosheath, a consequence of the MAVEN trajectory and the much smaller shock stand-off distance at Mars compared to Earth.

2.1.1. Field-Aligned Electron Energization and The Local Potential

In panel (d), we infer the local potential relative the upstream (defined as the reference potential of $\phi = 0$) from the field-aligned electron energization by comparing the phase space density of upstream solar wind electrons and local electrons. Theoretically, this procedure should be carried out with perfectly field-aligned electrons. In practice, however, we use a pitch angle (PA) range to approximate parallel (PA 0–45°) and antiparallel (PA 135°–180°) directions, as SWEA has a 22.5° angular resolution and also to increase counting statistics. More specifically, for each orbit, we identify a reference distribution function (DF), separately for the parallel and antiparallel directions, by averaging electron DFs for all measurements within a selected upstream region outside of the bow shock. This upstream region is defined as a region between two scaled shock fittings from Trotignon et al. (2006) with the semi-latus rectum L being 2.15 and 3 R_M, respectively, in comparison to an empirical L of 2.08 R_M, as shown in Figure S1 in the supporting information. Orbits without coverage in this upstream region will not be calculated for potentials. We have also tested with a PA width of 30° parallel/antiparallel to the magnetic field and the results were very similar, but more scattered. We thus only show results from a PA width of 45° in this study.

By applying the Liouville mapping, for field-aligned electrons, the energy change between the reference DF and the same local DF is the electron energization by an electrostatic potential. We average these energy differences, weighted by the variance in the measured flux, for energy channels within the 40–200 eV reference DF. This averaged energy difference is referred as the local potential (relative to the upstream). Note that this method relies on reasonable assumptions such as electrons being magnetized across the shock (e.g., Schwartz et al., 2011), and the electron spectral shape (within the selected energy range) not affected by the possible scattering by high-frequency plasma waves across the shock (e.g., Schwartz et al., 2019). All distributions are corrected for spacecraft potential, which is derived from the current-voltage (I-V) measurements from the Langmuir Probe and Waves (LPW) instrument (Andersson et al., 2015), available in the LPW L2 data product.

As shown in Figure 2c, the energy spectra of upstream solar wind (SW) electrons are stable and example DFs are shown as the red lines in panels (e) and (f) for parallel and antiparallel directions, respectively, while DFs in the magnetosheath, right at the top of the shock ramp (vertical green line), are shown as the black lines. In comparison, the shifted solar wind electron DFs by 160 eV (red lines) are also shown, which agree well with sheath electrons at energy ranges of 200–360 eV, validating the method of obtaining local potentials by comparing DFs. The DFs below ~40 eV for the shifted SW electrons and downstream electrons do not agree well, which will be discussed later. For this case study, the energy changes in parallel and antiparallel directions, thus the inferred local potentials, are about the same. Similarly, we calculate the
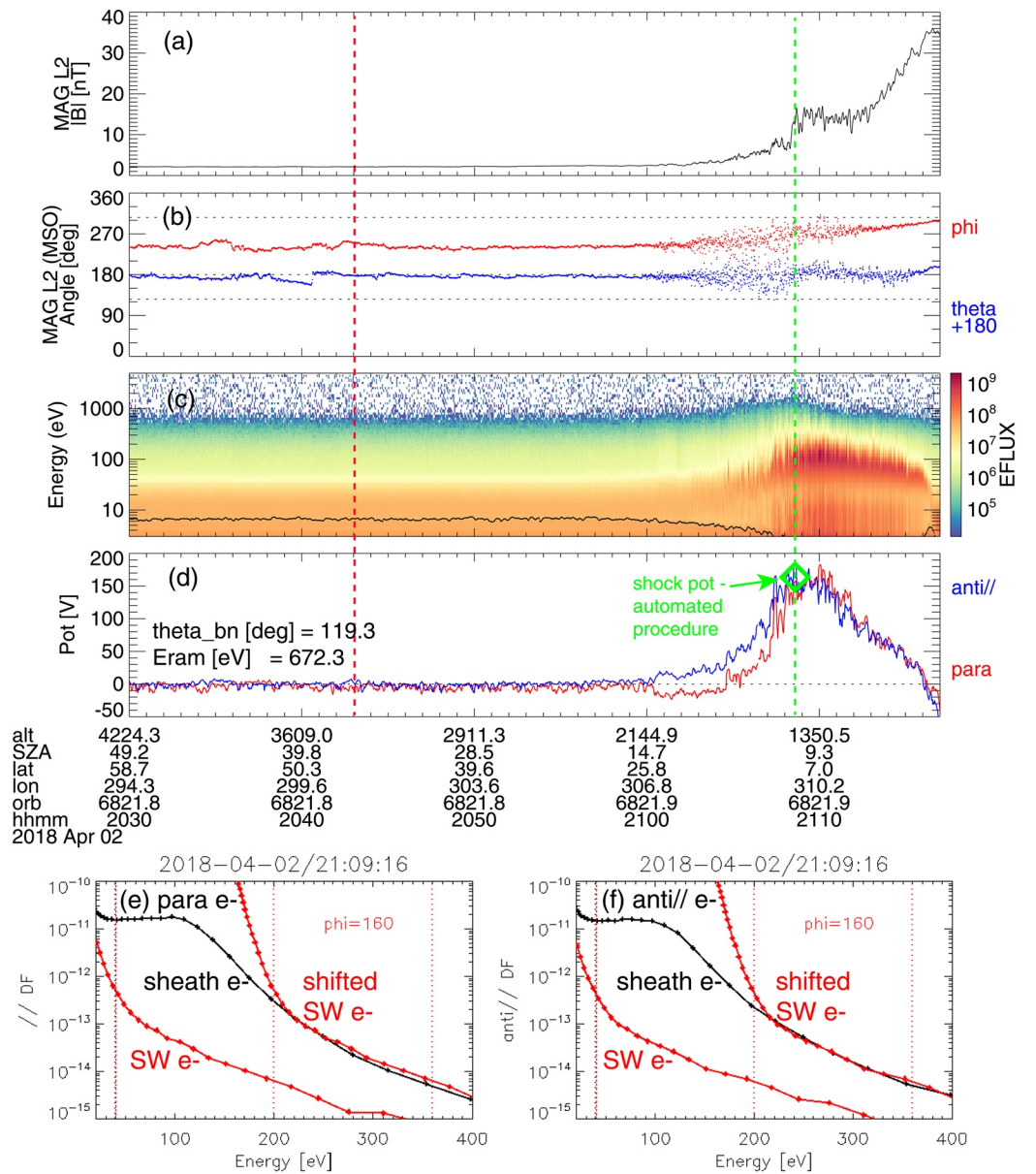
Figure 2. Time series of (a) magnetic field strength (nT, smoothed over 8s), (b) magnetic angles (°) in MSO coordinates, (c) omnidirectional electron energy spectra measured by SWEA, (d) local potentials derived from parallel (blue) and antiparallel (red) electrons. In (b), the red line is the angle from X to Y in MSO and the blue line is the angle relative to the Z axis in MSO but shifted by 180°. In (c), the black dotted line marks the spacecraft potential. In (d), the green diamond symbol is the derived shock location and shock potential and the green vertical line marks the shock location from the magnetic field strength. Panels (e) and (f) show the comparison of the phase space density (cm^{-3} (km/s)$^{-3}$) of upstream solar wind electrons (SW) and sheath electrons, as well as the shifted SW electrons by 160 eV, for parallel (PA 0–45°) and antiparallel (PA 135°–180°) directions, respectively, taken at times marked by the red and green vertical lines in the time series plot.

local potential relative to unperturbed upstream solar wind from parallel and antiparallel electrons for this orbit segment, shown as the blue and red lines in Figure 2d, respectively. The inferred potentials are about ~0 V in the upstream solar wind as expected, then increase sharply crossing the shock due to the cross-shock potential, peaking closely after the shock, and decrease further downstream. Schwartz et al. (2019) explained the weakening in electron energization as, further downstream, magnetic field lines on which electrons move intersect the bow shock at higher solar zenith angles (SZAs) where shock potentials are

weaker. The inferred negative potentials are invalid past the photoelectron boundary, as those are iono-spheric photoelectrons.

2.1.2. Cross-Shock Potentials

While we can derive a local potential for each orbit from both parallel and antiparallel electrons, cross-shock potentials should be more reliably inferred from electrons traveling from upstream to downstream. This is because we can reasonably assume the upstream solar wind electrons to be steady and the same whether the field lines connect to the shock or not. In contrast, electrons traveling from downstream to upstream are different from those in the unperturbed upstream solar wind. Obtaining potentials using these outgoing electrons requires ensuring that the reference solar wind distribution is taken on a field line that connects to the spacecraft. To distinguish electrons traveling upstream or downstream, we compute the angle (θ_{Bn}) between the shock normal, based on the shock fitting from Trotignon et al. (2006), and the upstream interplanetary magnetic field (IMF) direction. The upstream IMF direction is determined from MAG measurements and the upstream solar wind densities, temperatures, and velocities (V_p) are based on the measurements by the Solar Wind Ion Analyzer instrument (SWIA; Halekas et al. [2015]) in the upstream solar wind (Halekas et al., 2017). For $\theta_{Bn} > 90°$, parallel electrons cross the shock from upstream to downstream; for $\theta_{Bn} < 90°$, antiparallel electrons cross the shock from upstream to downstream.

To allow for searching through most of MAVEN orbits, we design an automated procedure to identify the shock potential, as well as the shock location. This is achieved by selecting 2% highest potentials inferred from electrons traversing the shock from upstream to downstream, which is then averaged to be the cross-shock potential, and the shock location is determined to be the highest altitude among the selected 2% potentials. The latter is to minimize dislocation of the shock, as electron observations, and thus potentials, are quite perturbed in the sheath. We emphasize that this study focuses on the cross-shock potentials, but not identifying the exact shock location. In fact, traditionally, studies (e.g., Schwartz et al., 1988) on Earth's shock potentials used values in a more stable downstream behind the shock, not necessarily right at the shock.

For our case study, $\theta_{Bn} = 119.3°$, thus the shock potential (ϕ in the spacecraft frame) is inferred from parallel electrons and determined to be $\sim$160 V, as indicated by the green diamond in Figure 2d, the same as the manually determined potential from Figure 2e. The inferred shock location is also about the same as the manually determined shock location (green vertical line). Shock potentials (ϕ) scale with the ram energy of upstream solar wind protons ($E_{\mathrm{ram}} = \frac{1}{2}m_p V_p^2$), which is determined to be 672 eV for this case study, which gives $\phi/E_{\mathrm{ram}} \sim 24\%$ at SZA $\sim 10°$.

2.1.3. Complication of HTF

Ideally, to obtain the most accurate shock potential in HTF, that is, ϕ^{HT}, we should transform electron energy and angular distributions into HTF for both upstream and downstream electrons. Assuming the first adiabatic invariant is conserved for electrons traversing the shock, this yields

$$\left(v_{//d} + U_{xd}\sec\theta_{Bnd}\right)^2 = \left(v_{//u} + U_{xu}\sec\theta_{Bnu}\right)^2 + v_{\perp u}^2\left(1 - \frac{B_d}{B_u}\right) + \frac{2e\phi^{HT}}{m_e} \tag{1}$$

where $v_{//}$ and $v_{\perp}$ are the electron peculiar velocity along and across the magnetic field line in the plasma rest frame (almost the same as the spacecraft frame for electrons >40 eV; Schwartz et al., 1988). Thus, the total parallel electron velocity ($v_{\perp u} = 0$) in HTF, relative to the bulk flow (field-aligned in HTF), is to apply a correction of $-U_x \sec\theta_{Bn}\hat{b}$ upstream and downstream, respectively (see Figure 1 above).

Such a correction to inferred ϕ in the spacecraft frame is estimated from Equation 1 to be $<\sim$20% for θ_{Bnu} $<70°$ or $> 110°$ for energy above 40 eV, as solar wind bulk flow ($\sim$400 km/s) is much smaller than the electron velocity (40 eV $\sim$ 3,800 km/s). In other words, as $\theta_{Bnd} > \theta_{Bnu}$ for fast shocks, our inferred ϕ is $<\sim$20%

lower than ϕ^{HT}, except for perpendicular shocks (i.e., $\theta_{Bnu} \sim 90°$). For simplicity, we approximate ϕ^{HT} with ϕ in this study without transforming to HTF for every orbit.

2.2. Case Studies: Overshoot

Our methodology identifies the maximum potential jump across the bow shock, which could, however, end up identifying the overshoot region, if present, just downstream of the shock, instead of the more traditional/stable downstream sheath region. Figure 3 shows two examples of such cases. In both cases, an overshoot can be identified by a peak in magnetic strength just downstream of the shock, followed by a roughly constant level further downstream, as shown in panels A1 and B1. Similarly, the local potential relative to the upstream, inferred from electrons traveling from upstream to downstream, has a peak roughly coincident with the overshoot and then decreases further downstream, as shown in panels A3 and B3. As mentioned above, this decreasing in potential further downstream manifests the time-history of solar wind flow carrying the IMF further downstream (Schwartz et al., 2019).

In these two cases, the overshoot potential is roughly twice of that further downstream of the overshoot. However, the lower potential further downstream is also partially caused by the IMF starting to intersecting the bow shock at higher SZAs. In other words, because of the small size of the Martian system (e.g., Mars' bow shock and the sheath behind), it is complicated to identify a value that can be tagged as downstream with any certainty, as the spatial gradients in all parameters are too strong to match directly with the classic textbook 1-D shock profile. Because of the complexity of differentiating overshoot and the more classical downstream region at Mars, in this study, we concentrate on the potential jump just downstream of the bow shock, occurring within the overshoot region more often than not.

3. Statistical Analyses of Cross-Shock Potentials

Case studies above demonstrate the reliability of our technique obtaining cross-shock potentials. We apply this technique to MAVEN from December 1, 2014 to November 30, 2019 and identify 8,718 shock crossings and shock potentials. As our defined upstream region (Figure S1) is based on an empirical bow shock fit but the bow shock location varies dynamically in reality, we calculate the averaged local potential within the selected upstream region ($\bar{\phi}_{up}$) for each orbit and exclude orbits when $|\bar{\phi}_{up}| > 10$ V. This criterion ensures that the reference electron energy spectrum is representative of upstream solar wind electron spectra. To separate the shock properties along IMF and across IMF, we also transform into a coordinate system such that the X-axis points from the Mars center to the Sun, the same as the MSO coordinate system, Y_P is collinear with the perpendicular IMF component ($\mathbf{B}_{\mathrm{perp}}$, w.r.t. X_{MSO}), and Z_P completes the right-handed system. Y_P is parallel to $\mathbf{B}_{\mathrm{perp}}$ for $Bx_{\mathrm{MSO}} < 0$ and antiparallel to $\mathbf{B}_{\mathrm{perp}}$ for $Bx_{\mathrm{MSO}} > 0$. In such a coordinate system, for a nominal Parker spiral IMF, the leading end of the IMF always aligns with positive Y_P and the trailing end with negative Y_P, preserving the structure of the bow shock with the quasi-parallel orientation on the negative Y_P side and the quasi-perpendicular orientation on the positive Y_P side for both away and toward IMF polarities. In short, the upstream IMF is in the $X - Y_P$ plane and Z_P is equivalent to the magnetic latitude. Note that, although Mars does not possess an intrinsic global dipole field, we use the term "magnetic latitude" to represent the solar zenith angle along the direction of the motional electric field for convenience.

Figure 4 shows the shock potentials mapped into the $X_{\mathrm{MSO}}-Y_P$ plane for $|Z_P| < 0.5$ R_M (top row) and the $X_{\mathrm{MSO}} - Z_P$ plane for $|Y_P| < 0.5$ R_M (bottom row), where R_M is the Mars radius. The left column shows the absolute potential value and the right column the normalized potential by the ram ion energy of upstream solar wind protons (E_{ram}). A few observations can be made. (1) The inferred shock locations agree well with the empirical fitting from Trotignon et al. (2006), validating of our automated procedure in identifying shock crossings. (2) Shock potentials peak near the subsolar region, with a value of $\sim$200 V and a ratio of $\sim$20% to the ram ion energy. This is because the shock potential is known to scale with the *normal* ram ion energy (to the shock surface; e.g., Schwartz et al., 1988; Thomsen et al., 1987), which becomes smaller at high SZAs. (3) The variation of shock potentials with SZA in the "magnetic equator" ($X_{\mathrm{MSO}} - Y_P$, Figures 4a and 4b) is similar to that with magnetic latitude (Figures 4c and 4d).
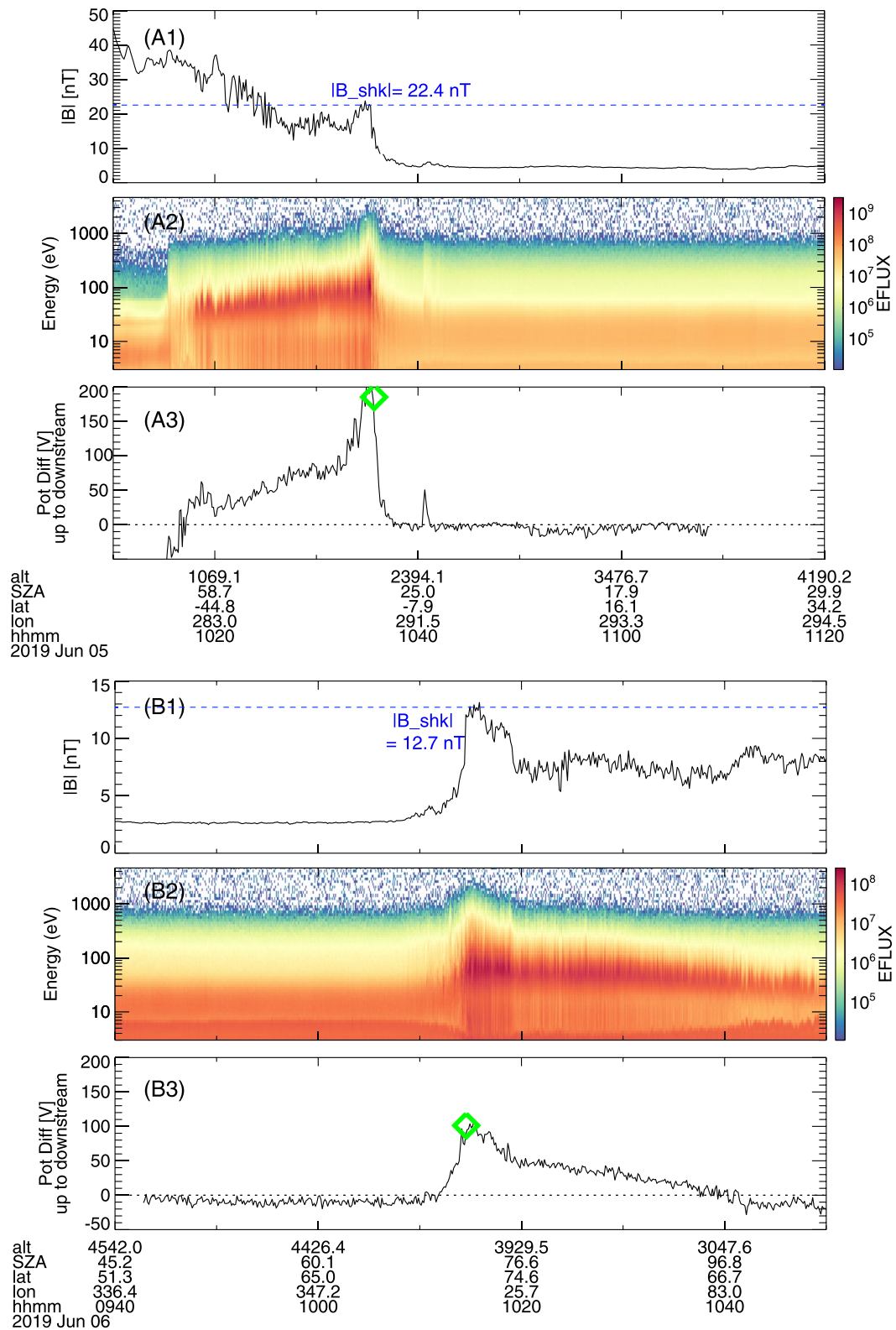
Figure 3. Time series of (A1, B1) magnetic field strength (nT, averaged for 8s), (A2, B2) omnidirectional electron energy spectra measured by SWEA, (A3, B3) local potentials derived from distribution functions of electrons traveling from upstream to downstream. Green diamonds are identified shock crossings and cross-shock potentials by our automated procedure. Identified magnetic strength at the shock B_{shk} from our automated procedure (Section 3) is given in panels A1 and B1.
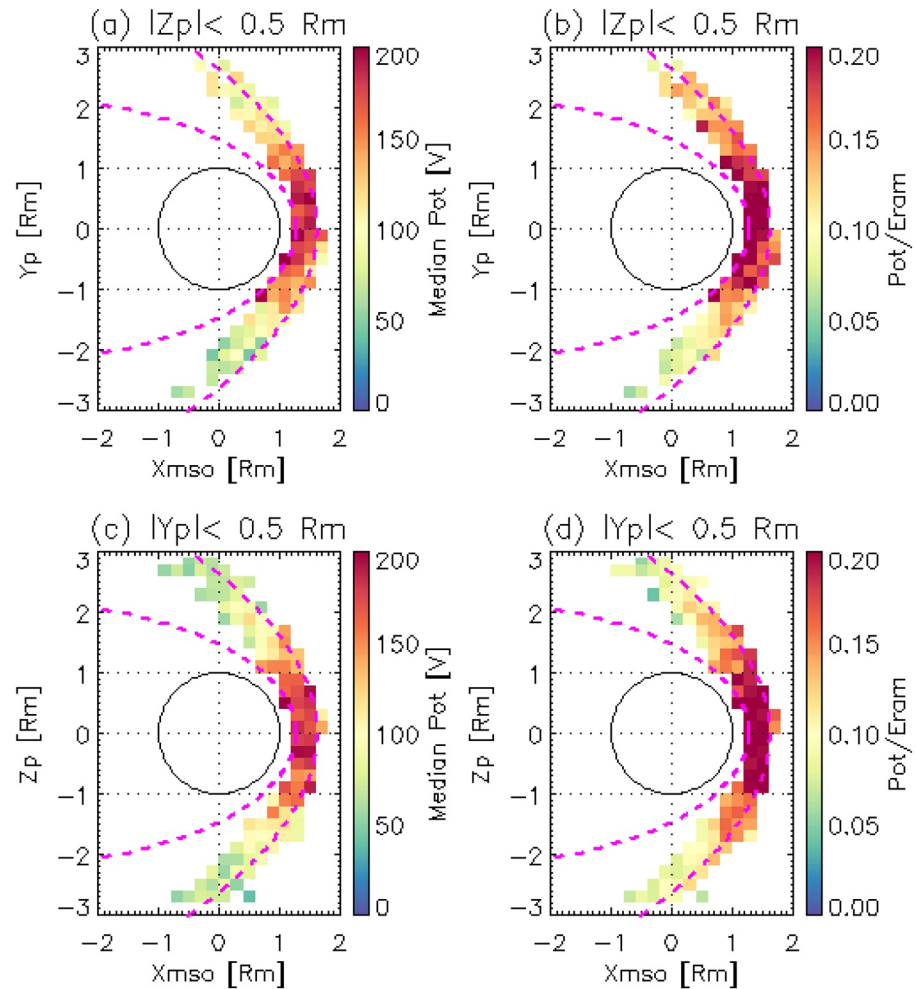
Figure 4. Shock potentials mapped into the $X_{\mathrm{MSO}} - Y_P$ plane for $|Z_P| < 0.5\ R_M$ (a) and the $X_{\mathrm{MSO}} - Z_P$ plane for $|Y_P| < 0.5\ R_M$ (c). The normalized shock potentials by the incident ram ion energy (E_{ram}) mapped into the $X_{\mathrm{MSO}} - Y_P$ plane for $|Z_P| < 0.5\ R_M$ (b) and the $X_{\mathrm{MSO}} - Z_P$ plane for $|Y_P| < 0.5\ R_M$ (d). The magenta dashed lines are the empirical fits of the bow shock and the magnetic pileup boundary from Trotignon et al. (2006).

It is worth noticing that our identified shock crossings are mostly located on the inner side of the empirical shock fitting, rather than being scattered on both sides. This is most likely caused by a solar cycle effect. Figure 5 shows the identified shock locations separated for times before (black) and after (blue) May 01, 2017 (a time roughly splitting the data set equally), representative of periods close to the solar maximum and minimum respectively. The blue crosses are signed with negative R_{mso} to be well separated from black crosses, where $R_{mso} = \sqrt{Y_{MSO}^2 + Z_{MSO}^2}$. As each time range spans over more than one Martian year, the seasonal effect (i.e., the Sun-Mars distance) is assumed to be averaged out. Shock locations (black crosses) are scattered on both sides of the empirical bow shock fitting for times close to the solar maximum, in contrast to located closer to the planet for times close to the solar minimum (blue crosses). This is expected as Mars' ionosphere is the main obstacle to the supersonic solar wind flow, which is much stronger during the solar maximum because of a higher extreme ultraviolet (EUV) irradiance. The ion pick-up process is expected to act much stronger to slow down the solar wind during the solar maximum. More specifically, with an increased EUV irradiance, the ionization of the neutrals increases as well, resulting in more mass loading of the solar wind. As a result, the solar wind energy exchange with more planetary ions leads to a decrease in energy (i.e., speed) of the solar wind and Mars' ionosphere thus becomes an effectively larger obstacle to the
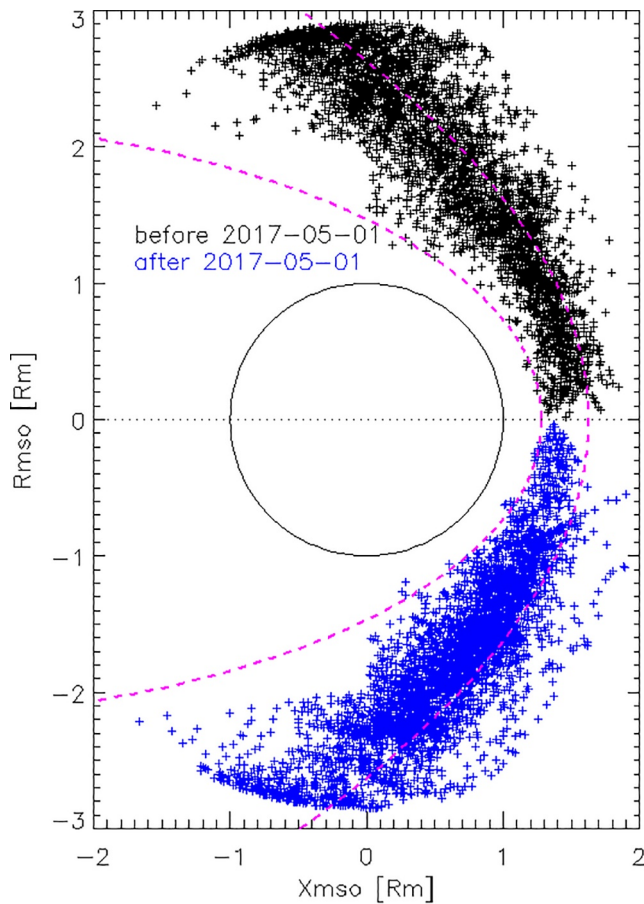
Figure 5. Identified shock locations in the MSO cylindrical coordinates for times before (black) and after (blue) May 01, 2017. The blue crosses are signed with negative R_{mso} to be well separated from black crosses, where $R_{mso} = \sqrt{Y_{MSO}^2 + Z_{MSO}^2}$.

solar wind. This is also in agreement with more distant shock locations during periods with a higher solar Lyman alpha emission, as revealed by Halekas et al. (2017).

To more quantitatively evaluate how the shock potential varies with SZA (reflecting the angle between the shock normal and the solar wind flow), we plot absolute potentials and normalized potentials as a function of SZA for $|Z_P| < 0.5\ R_M$ (a, b) and for $|Y_P| < 0.5\ R_M$ (c, d) in Figure 6. We also over-plot the variation of the absolute potential as $\phi_0 \cos^2\theta_n$ and the variation of the normalized potential as $r_0 \cos^2\theta_n$, where $\phi_0 = 200$ V is the estimated peak potential and $r_0 = 0.22$ the estimated peak ratio to the ram energy ($E_{\rm ram}$) at the subsolar region. θ_n is the calculated shock normal angle with respect to the X-axis at different SZAs, based on the shock fitting function from Trotignon et al. (2006). The variation of $\cos^2\theta_n$ arises from the conversion of the ram ion velocity, mainly in $-X_{\rm MSO}$, to the direction normal to the shock surface. The agreement between the median (blue) and mean (cyan) potentials and the theoretical variations (magenta) shows that the shock potential does vary with respect to SZA as the theory predicts. Note that we highlight cases where the transformation to HTF might be important (i.e., $70° < \theta_{Bnu} < 110°$) with green crosses in Figures 5–9. We find these cases are not that different from the rest of cases, implying that our approach of using potentials (ϕ) obtained in the spacecraft frame to approximate $\phi^{\rm HT}$ is not very problematic.

Theoretically (i.e., Equation 1), $\phi^{\rm HT}$ could have a dependence on the angle (θ_{bn}) between IMF and the shock normal vector. In Figure 7, we plot the normalized potential by $0.2E_{\rm ram}\cos^2\theta_n$ (to remove the dependence on $E_{\rm ram}$ and θ_n) against θ_{bn}. This normalized potential is, however, rather insensitive to θ_{bn}.

Except for ram ion energy, two upstream parameters that might affect the shock properties include the magnetosonic Mach number ($M_{\rm MS}$, for fast shocks) and the plasma beta (β). Here, we examine if/how they affect the cross-shock potentials. Figure 8 shows the shock potential as a function of $M_{\rm MS}$ (a, b) and β (c, d) for the subsolar region (SZA < 30°), minimizing the effect of θ_n. The calculation of magnetosonic Mach $M_{\rm MS}$ follows Halekas et al. (2017), assuming an electron temperature equal to the proton temperature and a polytropic index $\gamma = 5/3$. The shock potential ϕ has a somewhat positive correlation with $M_{\rm MS}$ (panel a) and $\log\beta$ (panel c) with correlation coefficients ~0.2. Meanwhile, $\phi/E_{\rm ram}$ weakly increases with $M_{\rm MS}$ (correlation coefficient ~0.3) but has little dependence on $\log\beta$ (correlation coefficient ~0).

One parameter related to the overshoot is the magnetic amplification across the shock, that is, the magnetic ratio just downstream of the bow shock to the upstream. We thus calculate the ratio of magnetic strength ($|B_{\rm shk}|$) at the shock and the upstream IMF amplitude ($|B_{\rm up}|$). $|B_{\rm shk}|$ is defined as the maximum magnetic amplitude (first smoothed for 16s to avoid large magnetic fluctuations near the shock) within 5 min upstream and downstream of the identified shock locations. This 10-min time window is to ensure we capture the maximum magnetic jump. Note that this $|B_{\rm shk}|$ will be the overshoot field, if exists, rather than the asymptotic downstream value. Figure 9 shows ϕ and $\phi/E_{\rm ram}$ against $|B_{\rm shk}|/|B_{\rm up}|$. We find a similar correlation between the shock potential and this magnetic ratio to $M_{\rm MS}$, as $M_{\rm MS}$ and $|B_{\rm shk}|/|B_{\rm up}|$ are highly correlated, as shown in Figure S2 in the supporting information.

4. Comparison of Shock Potentials at Mars and Earth

Comparing properties of shock potentials at Mars to that at Earth may provide an insight to similarities and differences in the formation of the bow shock at planets with mainly a significant ionosphere or a global intrinsic dipole field as an obstacle to the solar wind flow. The variation of $\phi/E_{\rm ram}$ against SZA and

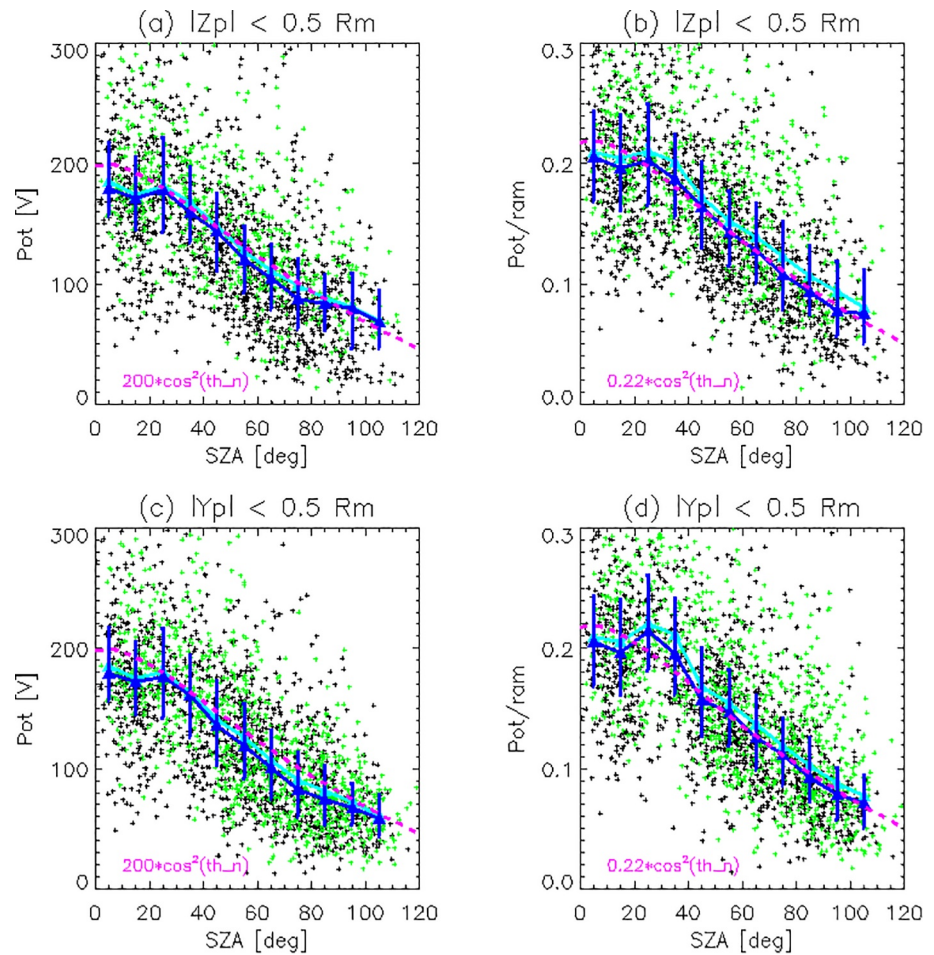**Figure 6.** Shock potentials against SZA for $|Z_P| < 0.5\ R_M$ (a) and for $|Y_P| < 0.5\ R_M$ (c). The normalized shock potentials by the incident ram ion energy (E_{ram}) against SZA for $|Z_P| < 0.5\ R_M$ (b) and for $|Y_P| < 0.5\ R_M$ (d). The blue lines and error bars are quartiles and the cyan lines are mean values. The magenta lines are for $200\cos^2\theta_n$ and $0.22\cos^2\theta_n$ in panels a, c and b, d, respectively. The green crosses are for $70° < \theta_{Bnu} < 110°$.
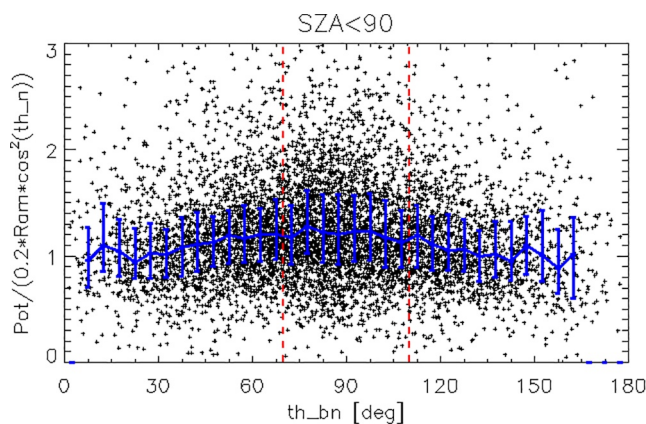

Figure 7. The ratio of shock potentials and a normalization factor ($0.2E_{ram}\cos^2(\theta_n)$) as a function of θ_{bn}, where E_{ram} is the ram ion energy of the upstream solar wind, θ_n is the normal angle of the shock surface, and θ_{bn} is the angle between the upstream IMF and the shock normal. The two vertical dashed lines mark 70° and 110°.

magnetic latitude found in this study is in agreement with that for Earth's bow shock (e.g., Schwartz et al., 1988). We also find ϕ/E_{ram} to be more or less insensitive to θ_{bn} and β, which is in agreement with findings from Schwartz et al. (1988) for Earth's bow shock. There are also disagreements. Near the subsolar region, or the shock nose, the shock potential is 200 V and has a $\phi/E_{ram} \sim 22\%$ on average. This ratio is significantly higher than the 10%–15% at Earth (Schwartz et al., 1988). In addition, a somewhat positive correlation between ϕ/E_{ram} and the magnetosonic Mach number found in our study is contradictory to a decreasing ratio with increasing Mach number at Earth (Schwartz et al., 1988). There are a few factors that might be responsible for these differences: (1) methodology, (2) overshoot, and (3) physical mechanisms.

4.1. Methodology

There is a significant difference between our approach in obtaining the shock potentials at Mars and that at Earth. Schwartz et al. (1988) presented two different methods. (1) Theoretically calculate the potential difference (ϕ_p) from the electron thermal pressure gradient across the shock
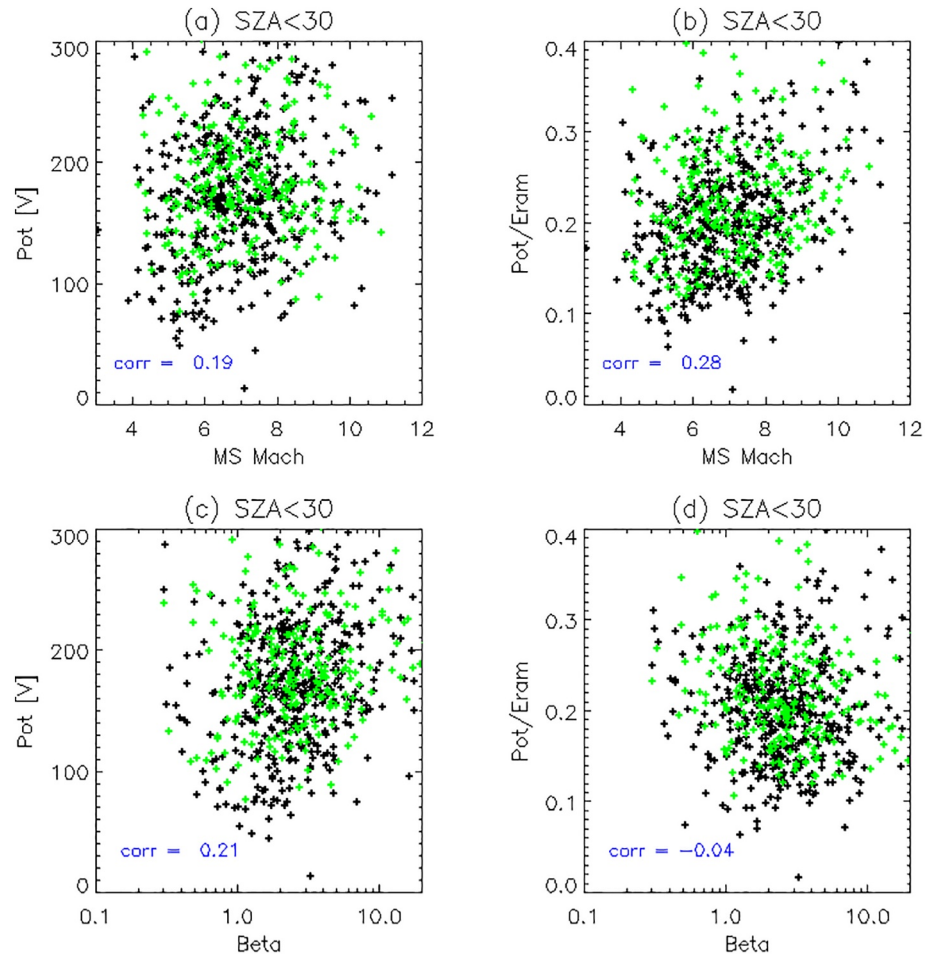
Figure 8. Shock potentials (the left column) and normalized shock potentials by the incident ram ion energy (E_{ram}) (the right column) for SZA < 30° against magnetosonic Mach numbers M_{MS} (a, b) and plasma beta β (c, d) of the upstream solar wind. The correlation coefficients of shock potentials and M_{MS} or $\log\beta$ are shown in the lower left corner of each panel. The green crosses are for $70° < \theta_{Bnu} < 110°$.
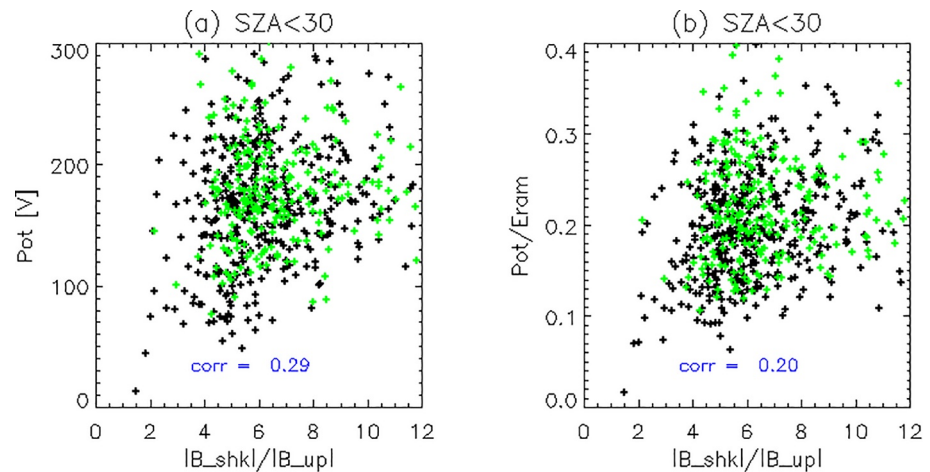

Figure 9. Shock potentials (a) and normalized shock potentials by the incident ram ion energy (E_{ram}) (b) for SZA < 30° against the ratio of the magnetic strengths at the identified shocks and the upstream IMF strength, $|B_{\text{shk}}|/|B_{\text{up}}|$. The correlation coefficients are shown in the lower left corner of each panel. The green crosses are for $70° < \theta_{Bnu} < 110°$.

with measured electron densities and temperatures, which gives $\phi_p/E_{ram} \sim 10\%$ at Earth. (2) Liouville mapping of the shoulder (edge of the flat top) in the shocked electron distribution back to the upstream solar wind electron distribution in the HTF, denoted as ϕ_{edge}, which gives $\phi_{edge}/E_{ram} \sim 15\%$. The second approach is essentially the same as our approach (denoted as ϕ_E) but we are using a higher energy range (40–200 eV upstream solar wind electrons). We applied these two methods to our case study and obtained $\phi_p \sim 70$ V and $\phi_{edge} \sim 110$ V. We also transformed spectra in Figure 2e into the HTF and then calculated the energy gain, which gave $\phi_E^{HT} \sim 165$ V, about the same as (only a 3% correction to) our simplified ϕ_E of 160 V. This comparison of different methods with our case study shows that $\phi_p/E_{ram} \sim 10\%$ and $\phi_{edge}/E_{ram} \sim 16\%$ at Mars are very similar to values at Earth and that our high ϕ_E/E_{ram} possibly arises from a higher energy range used to perform the Liouville mapping fit in our study.

There are arguments for each approach being more accurate but with its challenges. ϕ_p is theoretically correct but requires good estimates of electron density and temperature both upstream and downstream. Accurately estimating electron moments can be challenging in the sheath because of the secondaries produced within the instrument (mainly below 20 eV, as shown in Figure 2c). Note that for our case study, we assumed a flat top distribution below 30 eV to calculate electron moments, which is complicated to implement for all cases. A primary consequence of electron motion through ϕ^{HT} is the inflation of the distribution in energy and formation of a flat top at lower energies. The edge estimate ϕ_{edge} emphasizes the higher values of DF and also is closely related to the electron temperature, and hence ϕ_p. In our case, it is clear that some of the time (cf., Figure 2) the higher energy portions of DF upstream and downstream can be connected only by a constant potential (ϕ_E) that is higher than that found from ϕ_{edge}. It is possible that when the shock potential is large, the distribution function at low energies is also scattered in the process of filling in the phase space density hole, thus re-shaping DF at these edge energies. In contrast, high-energy electrons are less likely to be affected by this process and therefore are more appropriate for applying the Liouville mapping such that ϕ_E is a better estimate for the shock potential. We need to emphasize that, while ϕ and ϕ/E_{ram} can be different for different methodologies, the spatial variation and dependence on solar wind parameters of ϕ_E/E_{ram} found in this study are mostly the same as that for Earth's bow shock (e.g., Schwartz et al., 1988). It demonstrates the robustness of the overall findings of this study regardless of the methodology.

4.2. Overshoot

As pointed out in Section 2.2, our automated procedure identifies the maximum potential jump across the shock, which occurs within the overshoot region more often than not. In contrast, studies (e.g., Schwartz et al., 1988) on Earth's shock potentials use values in a more stable downstream behind the shock, excluding the overshoot region. From a few case studies, we find a ratio of 2–3 of the overshoot values to values further downstream. Lefebvre et al. (2007) reveals a similar ratio at Earth with a few case studies. In other words, high ϕ and ϕ/E_{ram} in this study may be partly because of overshoot. This might also explain the somewhat positive correlation between ϕ/E_{ram} and the magnetosonic Mach number found in this study. As overshoots occur more frequently at high Mach numbers, our potential estimates, if identified in the overshoot region, are more likely to be higher (than the typical downstream values), thus giving a positive trend between ϕ/E_{ram} and M_{MS}, as well as $|B_{shk}|/|B_{up}|$.

4.3. Physical Mechanisms

Mars' and Earth's shocks and their formations do differ in a few aspects. For example, Mars' shock surface is more curved and smaller than Earth's bow shock. Pick-up ions also play an important part in the shock formation at Mars. We then need to take into account different scale sizes at both planets, that is, the gyroradii of protons (and pick-up oxygens at Mars), the shock curvature, and the size of the magnetosheath. The thickness of the magneosheath is $\sim$0.5 R_M at Mars and $\sim$2–3 R_E at Earth near the subsolar region. A 1-keV proton in a 25-nT field, for example, has a gyroradius of nearly 200 km and pick-up oxygens at Mars have a typical gyroradius of a couple of Mars' radii in the sheath. In one gyroperiod of a proton, protons would traverse a big fraction of the magnetosheath at Mars but only a small fraction at Earth. This scale size difference means that at Earth there is time and space for the post-shock plasma to relax into more fluid-like while

at Mars solar wind protons and pick-up oxygens would behave more kinetic like. For the case of Mars, the downstream is governed by kinetic processes that occupy a good fraction of the sheath, which may feedback to the shock structure, for example, shock potentials. These differences might also partially be responsible for the differences in cross-shock potentials at Earth and Mars.

5. Conclusions

This study provides the first quantification and statistical analysis, to our best knowledge, of the cross-shock potential at Mars. We approximate the shock potential in the de Hoffmann-Teller frame (ϕ^{HT}) with the inferred shock potential in the spacecraft frame (ϕ) as we estimate the transformation is insignificant for most cases. More specifically, we infer ϕ from the energy change in the electron distribution function between upstream solar wind electrons and electrons just downstream the bow shock. Particularly, we compare distribution functions for electrons traveling from upstream to downstream, with the information of electron pitch angles, upstream IMF directions, and shock normal vectors (based on the empirical bow shock fitting from Trotignon et al. [2006]).

With an automated procedure, we identify 8,718 shock crossings based on MAVEN data from December 1, 2014 to November 30, 2019. As it is complicated to separate the overshoot region from the more stable downstream sheath at Mars because of a much smaller system, our inferred shock potentials are sometimes biased by overshoots. Statistically, we map the cross-shock potential in the magnetic equatorial plane and the plane of X_{mso} and magnetic latitude, strongest at the nose and weaker in the flanks. We also find a solar cycle effect on the shock location, closer to the planet for times closer to the solar minimum, as expected. Quantitatively, our results show that the shock potential varies similarly with SZA in the magnetic equatorial plane and also magnetic latitude, both as a function of $\cos^2\theta_n$, which is to convert the ram ion velocity to the direction normal to the shock surface. We then look at the dependence of the shock potential on other parameters and find no significant correlation with θ_{bn} and plasma beta β. Our results do reveal a somewhat positive correlation with the magnetosonic Mach number, contradictory to a decreasing ratio with increasing Mach number (and also $|B_{\mathrm{shk}}|/|B_{\mathrm{up}}|$) at Earth, which might be explained by the bias from potential values at the overshoot. Overall, our study provides the first detailed statistical analysis of the cross-shock potential at Mars and its dependence on several plasma parameters.

Lastly, we have discussed similarities and differences of cross-shock potentials at Mars and at Earth. We emphasize significant differences in the methodology in this study and Earth's research, as well as the overshoot effect on our results. The differences in Mars' and Earth's bow shocks and their formations, particularly different scale sizes, might also be partially responsible for the different trends in shock potentials at Mars and at Earth.

Data Availability Statement

The MAVEN data used in this study are available through the Planetary Data System (https://pds-ppi.igpp.ucla.edu/mission/MAVEN).

References

Andersson, L., Ergun, R., Delory, G., Eriksson, A., Westfall, J., Reed, H., et al. (2015). The Langmuir probe and waves (LPW) instrument for MAVEN. *Space Science Reviews*, *195*(1–4), 173–198. https://doi.org/10.1007/s11214-015-0194-3

Burne, S., Bertucci, C., Mazelle, C. X., Morales, L. F., Meziane, K., Espley, J. R., et al. (2020). *The structure of the Martian quasi-perpendicular supercritical shock as seen by MAVEN*. Earth and Space Science Open Archive, 23. Retrieved from https://doi.org/10.1002/essoar.10504776.1

Connerney, J., Espley, J., Lawton, P., Murphy, S., Odom, J., Oliversen, R., & Sheppard, D. (2015). The MAVEN magnetic field investigation. *Space Science Reviews*, *195*, 257–291.

Curry, S. M., Liemohn, M., Fang, X., Ma, Y., & Espley, J. (2013). The influence of production mechanisms on pick-up ion loss at mars. *Journal of Geophysical Research: Space Physics*, *118*(1), 554–569. https://doi.org/10.1029/2012ja017665

De Hoffmann, F., & Teller, E. (1950). Magneto-hydrodynamic shocks. *Physical Review*, *80*, 692–703. https://doi.org/10.1103/PhysRev.80.692

Dimmock, A., Balikhin, M., Krasnoselskikh, V., Walker, S., Bale, S., & Hobara, Y. (2012). A statistical study of the cross-shock electric potential at low Mach number, quasi-perpendicular bow shock crossings using Cluster data. *Journal of Geophysical Research*, *117*, A02210. https://doi.org/10.1029/2011ja017089

Feldman, W. C., Anderson, R. C., Bame, S. J., Gary, S. P., Gosling, J. T., McComas, D. J., et al. (1983). Electron velocity distributions near the Earth's bow shock. *Journal of Geophysical Research*, *88*(A1), 96–110. https://doi.org/10.1029/ja088ia01p00096

Formisano, V. (1974). The earth's bow shock fine structure. In D. E. Page (Ed.), *Correlated interplanetary and magnetospheric observations* (pp. 187–223). Dordrecht: Springer Netherlands.

Garnier, P., Steckiewicz, M., Mazelle, C., Xu, S., Mitchell, D., Holmberg, M. K. G., et al. (2017). The Martian photoelectron boundary as seen by MAVEN. *Journal of Geophysical Research: Space Physics*, *122*(10), 10472–10485. https://doi.org/10.1002/2017JA024497

Goodrich, C. C., & Scudder, J. D. (1984). The adiabatic energy change of plasma electrons and the frame dependence of the cross-shock potential at collisionless magnetosonic shock waves. *Journal of Geophysical Research*, *89*(A8), 6654–6662. https://doi.org/10.1029/ja089ia08p06654

Gruesbeck, J. R., Espley, J. R., Connerney, J. E. P., DiBraccio, G. A., Soobiah, Y. I., Brain, D., et al. (2018). The three-dimensional bow shock of Mars as observed by MAVEN. *Journal of Geophysical Research: Space Physics*, *123*(6), 4542–4555. https://doi.org/10.1029/2018ja025366

Halekas, J. S., Ruhunusiri, S., Harada, Y., Collinson, G., Mitchell, D. L., Mazelle, C., et al. (2017). Structure, dynamics, and seasonal variability of the Mars-solar wind interaction: MAVEN solar wind ion analyzer in-flight performance and science results. *Journal of Geophysical Research: Space Physics*, *122*(1), 547–578. https://doi.org/10.1002/2016ja023167

Halekas, J. S., Taylor, E., Dalton, G., Johnson, G., Curtis, D., McFadden, J., et al. (2015). The solar wind ion analyzer for MAVEN. *Space Science Reviews*, *195*(1–4), 125–151. https://doi.org/10.1007/s11214-013-0029-z

Hall, B. E. S., Sánchez-Cano, B., Wild, J. A., Lester, M., & Holmström, M. (2019). The Martian bow shock over solar cycle 23–24 as observed by the Mars express mission. *Journal of Geophysical Research: Space Physics*, *124*(6), 4761–4772. https://doi.org/10.1029/2018ja026404

Lefebvre, B., Schwartz, S. J., Fazakerley, A. F., & Décréau, P. (2007). Electron dynamics and cross-shock potential at the quasi-perpendicular Earth's bow shock. *Journal of Geophysical Research*, *112*, A09212. https://doi.org/10.1029/2007ja012277

Luhmann, J. (1986). The solar wind interaction with Venus. *Space Science Reviews*, *44*(3–4), 241–306. https://doi.org/10.1007/bf00200818

Mazelle, C., Meziane, K., Mitchell, D. L., Garnier, P., Espley, J. R., Hamza, A. M., et al. (2018). Evidence for neutrals-foreshock electrons impact at Mars. *Geophysical Research Letters*, *45*(9), 3768–3774. https://doi.org/10.1002/2018gl077298

Mazelle, C., Winterhalter, D., Sauer, K., Trotignon, J. G., Acuña, M. H., Baumgärtel, K., et al. (2004). Bow shock and upstream phenomena at Mars. In *Mars? Magnetism and its interaction with the solar wind* (pp. 115–181). Springer. https://doi.org/10.1007/978-0-306-48604-3_3

Meziane, K., Mazelle, C. X., Mitchell, D. L., Hamza, A. M., Penou, E., & Jakosky, B. M. (2019). A fast fermi acceleration at mars bow shock. *Journal of Geophysical Research: Space Physics*, *124*(7), 5528–5538. https://doi.org/10.1029/2019ja026614

Mitchell, D., Lin, R. P., Mazelle, C., Rème, H., Cloutier, P. A., Connerney, J. E. P., et al. (2001). Probing Mars' crustal magnetic field and ionosphere with the MGS electron reflectometer. *Journal of Geophysical Research*, *106*(E10), 23419–23427. https://doi.org/10.1029/2000je001435

Mitchell, D., Mazelle, C., Sauvaud, J.-A., Thocaven, J.-J., Rouzaud, J., Fedorov, A., et al. (2016). The MAVEN solar wind electron analyzer. *Space Science Reviews*, *200*(1–4), 495–528. https://doi.org/10.1007/s11214-015-0232-1

Nagy, A. F., Winterhalter, D., Sauer, K., Cravens, T. E., Brecht, S., Mazelle, C., et al. (2004). The plasma environment of Mars. In *Mars? Magnetism and its interaction with the solar wind* (pp. 33–114). Springer. https://doi.org/10.1007/978-0-306-48604-3_2

Savoini, P., Lembège, B., Krasnosselskhik, V., & Kuramitsu, Y. (2005). Under and over-adiabatic electrons through a perpendicular collisionless shock: Theory versus simulations. *Annales Geophysicae 23*, 3685–3698.

Schwartz, S. J., Andersson, L., Xu, S., Mitchell, D. L., Akbari, H., Ergun, R. E., et al. (2019). Collisionless electron dynamics in the magnetosheath of Mars. *Geophysical Research Letters*, *46*(21), 11679–11688. https://doi.org/10.1029/2019gl085037

Schwartz, S. J., Henley, E., Mitchell, J., & Krasnoselskikh, V. (2011). Electron temperature gradient scale at collisionless shocks. *Physical Review letters*, *107*(21), 215002. https://doi.org/10.1103/physrevlett.107.215002

Schwartz, S. J., Thomsen, M. F., Bame, S. J., & Stansberry, J. (1988). Electron heating and the potential jump across fast mode shocks. *Journal of Geophysical Research*, *93*(A11), 12923–12931. https://doi.org/10.1029/JA093iA11p12923

Scudder, J. D., Mangeney, A., Lacombe, C., Harvey, C. C., Wu, C. S., & Anderson, R. R. (1986). The resolved layer of a collisionless, high β, supercritical, quasi-perpendicular shock wave: 3. Vlasov electrodynamics. *Journal of Geophysical Research*, *91*(A10), 11075–11097. https://doi.org/10.1029/ja091ia10p11075

Thomsen, M. F., Mellott, M. M., Stansberry, J. A., Bame, S. J., Gosling, J. T., & Russell, C. T. (1987). Strong electron heating at the Earth's bow shock. *Journal of Geophysical Research*, *92*(A9), 10119–10124. https://doi.org/10.1029/ja092ia09p10119

Trotignon, J. G., Mazelle, C., Bertucci, C., & Acuña, M. H. (2006). Martian shock and magnetic pile-up boundary positions and shapes determined from the Phobos 2 and Mars Global Surveyor data sets. *Planetary and Space Science*, *54*(4), 357–369. https://doi.org/10.1016/j.pss.2006.01.003

Vignes, D., Mazelle, C., Rme, H., Acuña, M. H., Connerney, J. E. P., Lin, R. P., et al. (2000). The solar wind interaction with Mars: Locations and shapes of the bow shock and the magnetic pile-up boundary from the observations of the MAG/ER Experiment onboard Mars Global Surveyor. *Geophysical Research Letters*, *27*, 49–52. https://doi.org/10.1029/1999GL010703

Wilkinson, W. P. (2003). The Earth's quasi-parallel bow shock: Review of observations and perspectives for Cluster. *Planetary and Space Science*, *51*(11), 629–647. https://doi.org/10.1016/s0032-0633(03)00099-0

Xu, S., Mitchell, D. L., McFadden, J. P., Fillingim, M. O., Andersson, L., Brain, D. A., et al. (2020). Inverted-V electron acceleration events concurring with localized auroral observations at Mars by MAVEN. *Geophysical Research Letters*, *47*(9), e2020GL087414. https://doi.org/10.1029/2020GL087414

Xu, S., Poppe, A. R., Halekas, J. S., Mitchell, D. L., McFadden, J. P., & Harada, Y. (2019). Mapping the lunar wake potential structure with ARTEMIS data. *Journal of Geophysical Research: Space Physics*, *124*(5), 3360–3377. https://doi.org/10.1029/2019ja026536